Chemical Geology 483 (2018) 332–341

Contents lists available at ScienceDirect

Chemical Geology

journal homepage: www.elsevier.com/locate/chemgeo

Invited research article

Revealing mineralization and subsequent hydrothermal events: Insights from $^{40}Ar/^{39}Ar$ isochron and novel gas mixing lines of hydrothermal quartzs by progressive crushing

Xiu-Juan Bai[a], Ying-De Jiang[b], Rong-Guo Hu[c], Xiang-Ping Gu[d], Hua-Ning Qiu[a,b,*]

[a] Key Laboratory of Tectonics and Petroleum Resources (China University of Geosciences Wuhan), Ministry of Education, Wuhan 430074, China
[b] State Key Laboratory of Isotope Geochemistry, Guangzhou Institute of Geochemistry, Chinese Academy of Sciences, Guangzhou 510640, China
[c] College of Earth Sciences and Guangxi Key Laboratory of Hidden Metallic Ore Deposits Exploration, Guilin University of Technology, Guilin 541004, China
[d] School of Geosciences and Info-Physics, Central South University, Changsha 410012, China

ARTICLE INFO

Editor: D.B. Dingwell

Keywords:
$^{40}Ar/^{39}Ar$ crushing technique
Gas mixing line
Fluid inclusion
Tungsten mineralization age
Inverse isochron

ABSTRACT

Increasingly more data have indicated that the $^{40}Ar/^{39}Ar$ crushing technique provides a very useful approach to determine the mineralization ages of hydrothermal ore deposits. In this study novel gas mixing lines are proposed based on the data of two quartz samples by $^{40}Ar/^{39}Ar$ crushing. Electron microprobe analyses indicate that the quartz grains contain K-rich silicate microlites. Both quartzs by crushing yield two mixing lines with ages corresponding respectively to those of K-feldspar or sericite (post-mineralization fluids) and muscovite samples (ore-forming fluids). This is the first report that both ages of secondary and primary fluid inclusions (SFIs and PFIs) are confirmed correspondingly by those of the K-rich minerals. This study strongly indicates that the $^{40}Ar/^{39}Ar$ crushing technique is very useful to determine the ages of geofluid activities. The newly proposed gas mixing patterns are shown on the inverse and normal isochron diagrams, indicating: (1) the mixtures are in different proportions of the PFIs and SFIs in different crushing steps; (2) the gas mixing lines yield PFI ages with low initial $^{40}Ar/^{36}Ar$ ratios; (3) an intermediate age between PFI and SFI ages cannot be obtained because the progressive crushing technique never release gas mixtures with a constant PFI/SFI proportion for each step. The gas mixing lines are thus interpreted to yield significant geological ages. The mixing patterns will help us better understand the $^{40}Ar/^{39}Ar$ dating results and be used for references to other isotopic mixing isochron systems.

1. Introduction

The mineralization age is very important for understanding the genesis of a hydrothermal ore deposit. However, it is not easy to determine mineralization ages of the Au, Cu, Pb and Zn ore deposits because of the lack of suitable minerals for traditional isotopic geochronological methods. Increasing attention has focused on fluid inclusions in an attempt to find a widely applicable method to determine ore-forming ages since 1980s by the Rb–Sr method Shepherd and Darbyshire (1981) and $^{40}Ar/^{39}Ar$ method (Kelley et al., 1986; Qiu and Dai, 1989). An inline crushing technique has been used to extract the fluid inclusions for $^{40}Ar/^{39}Ar$ dating. Many successful applications of the $^{40}Ar/^{39}Ar$ crushing method for different types of minerals have been reported, such as quartz (Kendrick et al., 2001; Qiu, 1996; Qiu et al., 2002; Turner and Bannon, 1992; Turner and Wang, 1992), pyrite (Phillips and Miller, 2006), sphalerite (Jiang et al., 2012; Qiu and Jiang, 2007), cassiterite and wolframite (Bai et al., 2013). Apart from dating fluid inclusions of hydrothermal deposits, the $^{40}Ar/^{39}Ar$ crushing technique has also been successfully applied to determine the fluid inclusions within garnet and amphibole of (U)HP metamorphic rocks (Qiu and Wijbrans, 2006; Qiu and Wijbrans, 2008; Qiu et al., 2010), and skarn-related scapolite (Kendrick and Phillips, 2009). Furthermore, it is astounding to creatively apply this technique to determine natural gas emplacement (Qiu et al., 2011; Yun et al., 2010) and hydrocarbon accumulation (Liu et al., 2011).

Quartz is a ubiquitous mineral formed by intermediate-acid magmas and various geological fluids, such as hydrothermal, magmatic, metamorphic and tectonic fluids. The transparency of quartz makes it easy to observe and measure the shapes, homogenization and freezing temperatures of fluid inclusions under a microscope. The low radioactivity of irradiated quartz, much lower than that of irradiated cassiterite, wolframites, sphalerite and other sulfide minerals, makes it convenient to handle the quartz samples during the experiments and to deal with the crushed quartz powder after analyses. Many significant quartz

* Corresponding author at: Key Laboratory of Tectonics and Petroleum Resources (China University of Geosciences Wuhan), Ministry of Education, Wuhan 430074, China.
E-mail address: huaningqiu@cug.edu.cn (H.-N. Qiu).

https://doi.org/10.1016/j.chemgeo.2018.02.039
Received 3 September 2017; Received in revised form 6 January 2018; Accepted 27 February 2018
Available online 06 March 2018
0009-2541/

$^{40}Ar/^{39}Ar$ data have been obtained from hydrothermal deposits, metamorphic and tectonic quartz veins. Therefore, quartz is the most important mineral for the $^{40}Ar/^{39}Ar$ crushing analyses.

To better understand the K–Ar system of the mineral assemblages of tungsten ores, paragenetic muscovite, wolframite, and quartz were selected for $^{40}Ar/^{39}Ar$ dating. The small K-feldspar veins cutting the ores were also collected to constrain on the post-mineralization hydrothermal activities that formed the secondary fluid inclusions or K-feldspar microcrystals within the minerals of ores (cassiterite, wolframite, molybdenite and quartz), which may affect the $^{40}Ar/^{39}Ar$ dating results of the primary fluid inclusions within the ore minerals. In the case of subsequent geofluid overprinting, can we still obtain significant $^{40}Ar/^{39}Ar$ ages by crushing for these ore minerals? We proposed a gas mixing release pattern to explain wolframite $^{40}Ar/^{39}Ar$ dating results corresponding to normal isochron age with unexpectedly low initial $^{40}Ar/^{36}Ar$ ratio (Fig. 9 of Bai et al., 2013). Now we examine more samples by $^{40}Ar/^{39}Ar$ crushing with electron microprobe analyses, to further elaborate and reveal the significance of the mixing lines obtained from quartz samples by $^{40}Ar/^{39}Ar$ crushing.

2. Geological setting and samples

We selected the samples from the Piaotang and Niuling tungsten deposits, Dayu County, Jiangxi Province, southern China (see Fig. 1 of Bai et al., 2013). Piaotang tungsten deposit is a large-scale quartz-vein-type tungsten polymetallic deposit (He et al., 2010), associated with a granite within the well-known South China Tungsten Metallogenic Province (Li, 2011; Liu and Yu, 2011; Liu et al., 2014; Wang et al., 2010), geologically in the northern section of Xihuashan-Zongshukeng NNE Chongyi-Dayu-Shangyou tungsten-tin polymetallic mineralization belt. Niuling deposit is a medium-size deposit in the inner contact zone of a granite. The ore minerals of Piaotang and Niuling tungsten deposits are mainly composed of wolframite, some cassiterite and molybdenite, and minor bismuthinite, chalcocite, galena and sphalerite. The gangue minerals include quartz, K-feldspar, fluorite and muscovite. The wolframite, molybdenite and quartz are in large crystal sizes (> 10 mm). Small K-feldspar veins cut the wolframite and quartz in the ores (Fig. 1). In this study, the single mineral samples are separated from the quartz-vein-type tungsten ores, except for the hand-specimen 09NL01 of a mineralization-related granite.

There are abundant fluid inclusions within the quartz crystals used in this study (Fig. 2). The primary fluid inclusions of quartz 09PT37Q are mainly elliptical (5–10 μm) and round (< 5 μm) in shape; and those of 09NL05Q are mainly rectangular (8–15 μm) and square (< 10 μm) in shape. It is easy to observe bubbles moving inside the big fluid inclusions. The secondary fluid inclusions are distributed along microcracks in the quartz crystals.

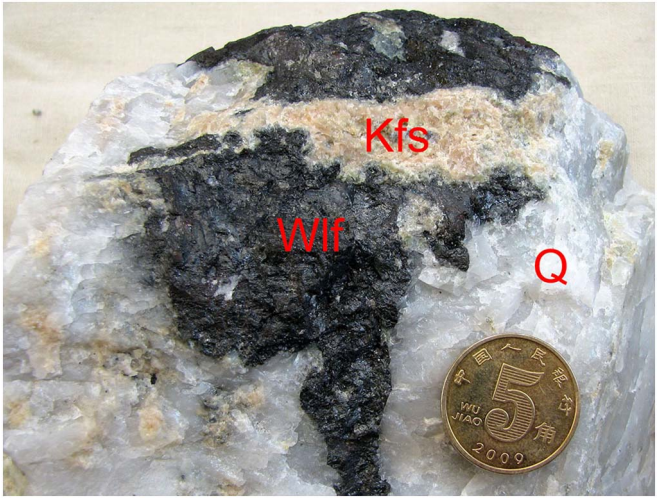

Fig. 1. Photo of a quartz-vein-type tungsten ore from Piaotang, showing post-mineralization K-feldspar veins cutting wolframite and quartz. Q: quartz; Wlf: wolframite; Kfs: K-feldspar.

3. Analytical methods

3.1. Electron microprobe analyses

In order to correctly interpret the quartz $^{40}Ar/^{39}Ar$ dating results by crushing, potential K-bearing minerals with the quartz samples were detected on a JEOL JXA-8100 electron probe microanalyser (EPMA), equipped with four wavelength-dispersive spectrometers (WDS), at the State Key Laboratory of Geological Processes and Mineral Resources, China University of Geosciences (Wuhan). The EPMA was operated at an accelerating voltage of 15 kV with a beam current of 10 nA and a 1–10 μm focused electron beam. Data were corrected on-line using a modified ZAF (atomic number, absorption, fluorescence) correction procedure. Element peaks and backgrounds were measured for all elements with counting times of 10 s and 5 s. The following standards were used: Sanidine (K), Pyrope Garnet (Fe), Diopsode (Ca), Jadeite (Na), Diopsode (Mg) and Pyrope Garnet (Al), Rhodonite (Mn), Jadeite (Si), Rutile (Ti).

3.2. $^{40}Ar/^{39}Ar$ analyses

Hand specimens were individually crushed in a stainless steel mortar and then sieved. Grains were sieved from 30 to 60 mesh (0.50–0.25 mm). Single mineral grains were carefully separated by hand picking under a binocular microscope and then cleaned in an ultrasonic bath with deionized water for 15 min. Samples packed in aluminum foil, together with the flux monitor ZBH25 biotite packed in copper foil, were put into aluminum tubes, then irradiated for 48 h in the Beijing 49-2 reactor. The ZBH25 biotite by $^{40}Ar/^{39}Ar$ step heating formed a flat age spectra with a plateau age of 132.7 ± 0.1 Ma (1σ), carried out in the Australian National University (Wang, 1983).

The argon isotopes were analysed on a GVI-5400® noble gas mass spectrometer in the State Key Laboratory of Isotope Geochemistry, Guangzhou Institute of Geochemistry, Chinese Academy of Sciences. The fluid inclusions were extracted in a crushing apparatus (Qiu and Jiang, 2007; Qiu et al., 2011) connected to the purification system and mass spectrometer. Prior to experiments, the extraction and purification systems were baked with heating tapes in order to reduce the system blanks. The sample in the crusher was heated by a temperature-controlled furnace at 150 °C for ca. 10 h. In order to correct the system blanks, cool blanks were carried out at the start and end of each sample experiment, and between every four to six steps of sample analyses. The released gases were firstly cleaned up through the cryotrap (−100 °C) to absorb the moisture from fluid inclusions, then further purified using two SAES NP10 Zr/Al getters at ~ 400 °C and at room temperature respectively, resulting in purified noble gases for argon isotope analyses in the mass spectrometer.

Correction factors for interfering argon isotopes derived from irradiated CaF_2 and K_2SO_4 are $(^{39}Ar/^{37}Ar)_{Ca} = 8.984 \times 10^{-4}$, $(^{36}Ar/^{37}Ar)_{Ca} = 2.673 \times 10^{-4}$ and $(^{40}Ar/^{39}Ar)_{K} = 5.97 \times 10^{-3}$. The $^{40}Ar/^{39}Ar$ results were calculated and plotted using the software ArArCALC (Version 2.4) (Koppers, 2002).

4. Results

4.1. Electron microprobe analyses

The back scattered electron (BSE) images and K-Kα X-ray images of the quartz samples indicate that some K-rich silicate microcrystals (5–20 μm) existing inside quartz grains (Fig. 3). The chemical compositions of the K-rich minerals were further analysed with WDS EPMA.

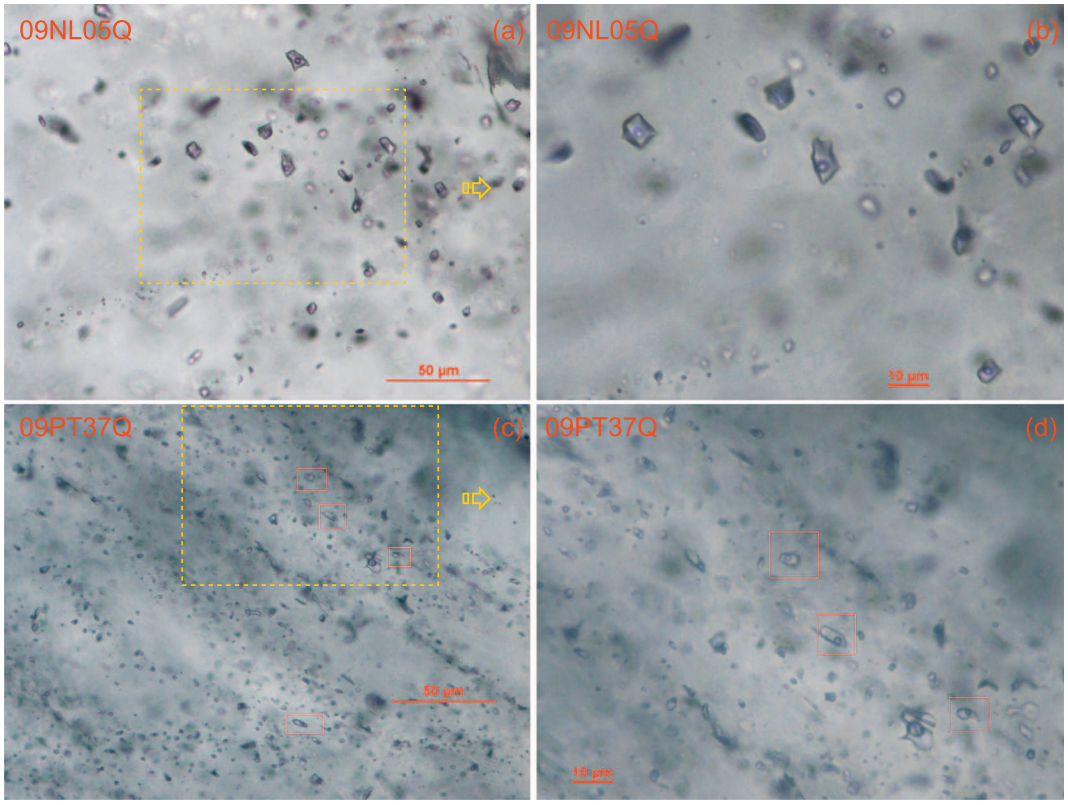

Fig. 2. Photomicrographs of 09NL05Q (a & b) and 09PT37Q (c & d) showing the fluid inclusions inside the quartz samples.

The WDS results of spot A in 09PT37Q are: Na_2O 0.148%, K_2O 16.538%, FeO 0.032%, Al_2O_3 17.929%, TiO_2 0.010% and SiO_2 67.106%; Spot B in 09NL05Q: Na_2O 0.651%, K_2O 15.701%, CaO 0.018%, Al_2O_3 17.816%, SiO_2 64.828%; Spot C in 09NL05Q: Na_2O 0.173%, K_2O 10.909%, FeO 6.865%, MgO 0.134%, MnO 0.828%, Al_2O_3 28.225%, SiO_2 47.500%. Based on these chemical compositions, the K-rich minerals of spots A and B are probably K-feldspar, and spot C white mica.

4.2. $^{40}Ar/^{39}Ar$ dating results

The K-rich minerals of muscovite, K-feldspar and sericite were analysed by $^{40}Ar/^{39}Ar$ laser stepwise heating. The fluid inclusions in quartz samples were extracted by crushing in vacuo. All $^{40}Ar/^{39}Ar$ dating results are summarized in *the supplementary file* of the Microsoft Excel sheets. The argon isotope intensities and their uncertainties are expressed throughout in volts. All analytical uncertainties are provided at 2σ in this paper.

4.2.1. Ore muscovite $^{40}Ar/^{39}Ar$ heating

Muscovite samples 09NL05Ms and 09PT37Ms from tungsten ores by $^{40}Ar/^{39}Ar$ laser stepwise heating form very flat age spectra covering 100% ^{39}Ar released, with well-concordant plateau and isochron ages (Fig. 4). Their ages for 09NL05Ms and 09PT37Ms are 159.5 ± 1.5 Ma and 157.2 ± 1.5 Ma respectively, representing the tungsten mineralization ages in Niuling and Piaotang.

4.2.2. Sericite and K-feldspar $^{40}Ar/^{39}Ar$ heating

The sericite 09NL01Ser from altered metallogenic granite in Niuling yields relatively complicated age spectrum by laser stepwise heating (Fig. 5). The apparent ages increase from 98.4 Ma to 130.4 Ma during the first three steps, followed by a plateau of 137.3 ± 1.4 Ma (MSWD = 3.9) comprising 10 steps with 80.1% ^{39}Ar released, and finally descended to 133.3 Ma and 132.4 Ma at the last two steps.

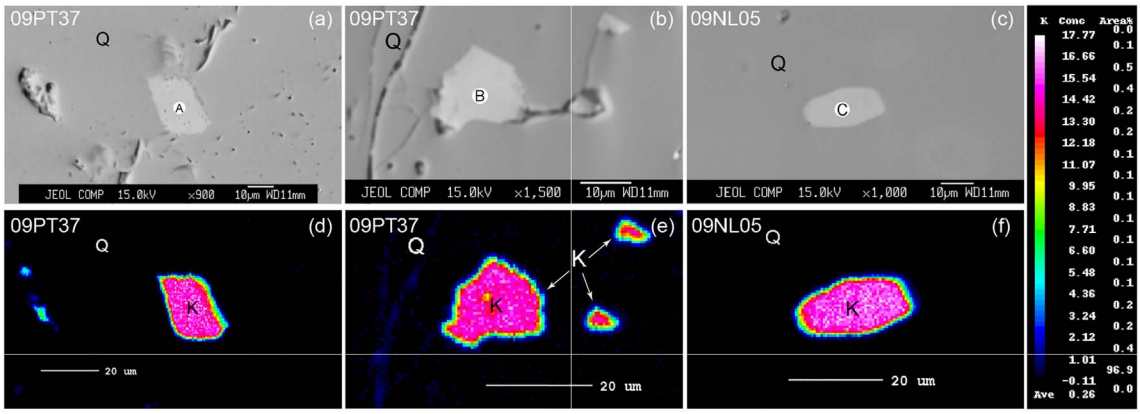

Fig. 3. BSE and K-Kα X-ray images of 09PT37Q and 09NL05Q. Q: quartz; K: potassium-rich microcrystals.

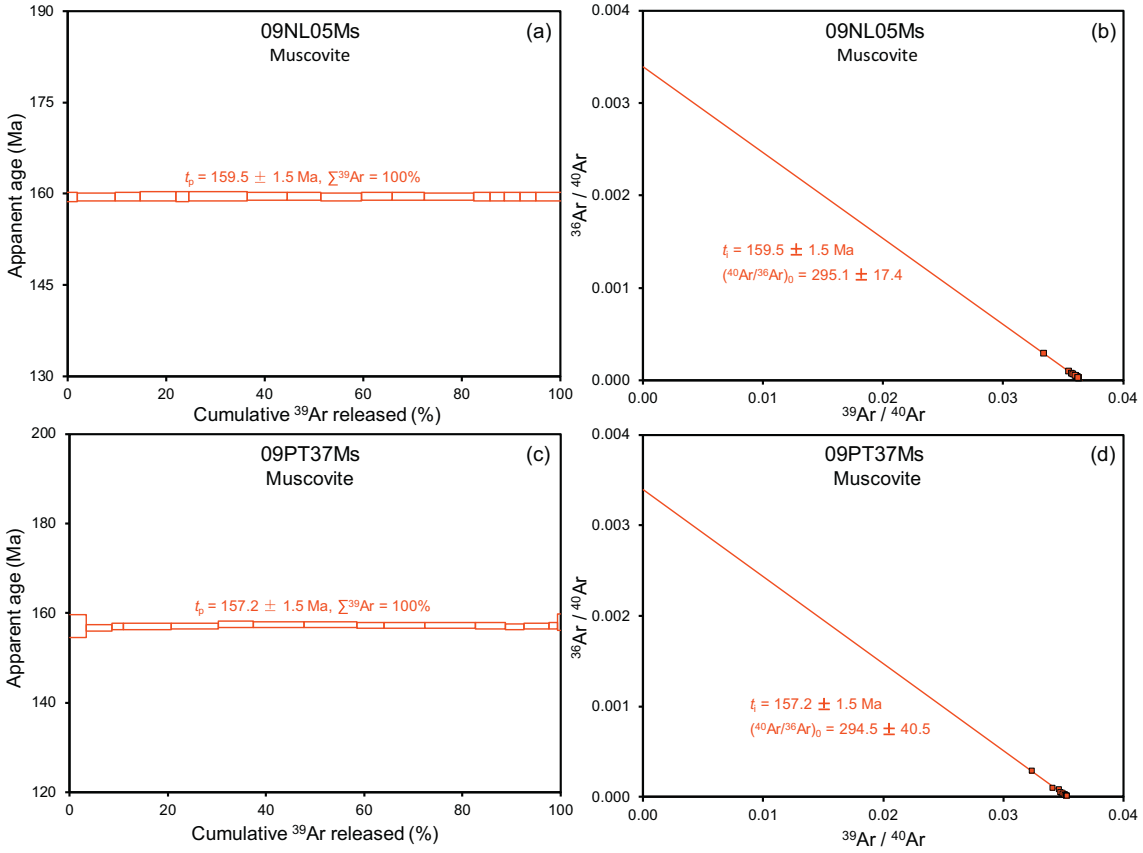

Fig. 4. Plots of ^{40}Ar/^{39}Ar age spectra and inverse isochron lines of muscovite samples 09NL05Ms and 09PT37Ms by laser stepwise heating.

Furthermore, the data points of the age plateau well define an isochron of 137.6 ± 1.6 Ma (MSWD = 3.9) in concordance with the plateau age.

All three K-feldspars samples of 09PT12Kfs, 09PT42Kfs and 09PT43Kfs in Piaotang by ^{40}Ar/^{39}Ar laser stepwise heating yield very flat spectra (Fig. 6a, c, e) with the plateau ages of 83.0 ± 0.8 Ma (MSWD = 0.03), 82.2 ± 0.8 Ma (MSWD = 0.1) and 82.3 ± 0.8 Ma (MSWD = 0.4), except for the first steps. Their corresponding isochron ages are 83.0 ± 0.8 Ma (MSWD = 0.03), 82.2 ± 1.0 Ma (MSWD = 0.2) and 81.6 ± 2.1 Ma (MSWD = 0.4) (Fig. 6b, d, f) respectively, indistinguishable from the plateau ages.

The ages of the sericite and K-feldspar samples are much younger than those of the ore muscovites, confirming that they were produced by postmineralization fluids rich in potassium in Niuling and Piaotang. The postmineralization K-rich fluids would also have formed some secondary fluid inclusions (Fig. 2) and even K-rich microcrystals (Fig. 3) within the previously-formed wolframite and quartz (Fig. 1). Can we still obtain the ore-forming ages for the wolframites and quartzs by ^{40}Ar/^{39}Ar crushing in this case? A wolframite case was preliminarily shown in our previous paper (Bai et al., 2013). Now two quartz samples will be further discussed.

4.2.3. *Quartz ^{40}Ar/^{39}Ar crushing*

4.2.3.1. 09NL05Q. This sample was crushed in 24 steps with a total number of pestle drops of 18,443. A monotonously declining age spectrum is obtained from the experiment (Fig. 7a, dark solid line). The first two steps released most excess ^{40}Ar (^{40}Ar$_{ex}$) with abnormally old apparent ages of > 2000 Ma, followed by decreasing apparent ages from 1300 Ma at step 3 to 167 Ma at step 9. In the final steps the apparent ages decreased slowly from 158.3 Ma at step 10 to 141.1 Ma at

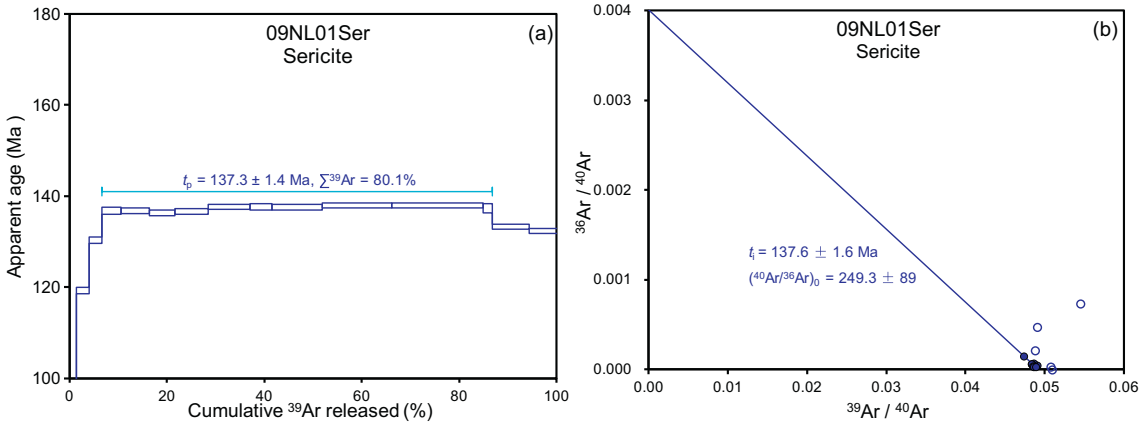

Fig. 5. Plots of ^{40}Ar/^{39}Ar age spectrum and inverse isochron line of sericite 09NL01Ser by laser stepwise heating.

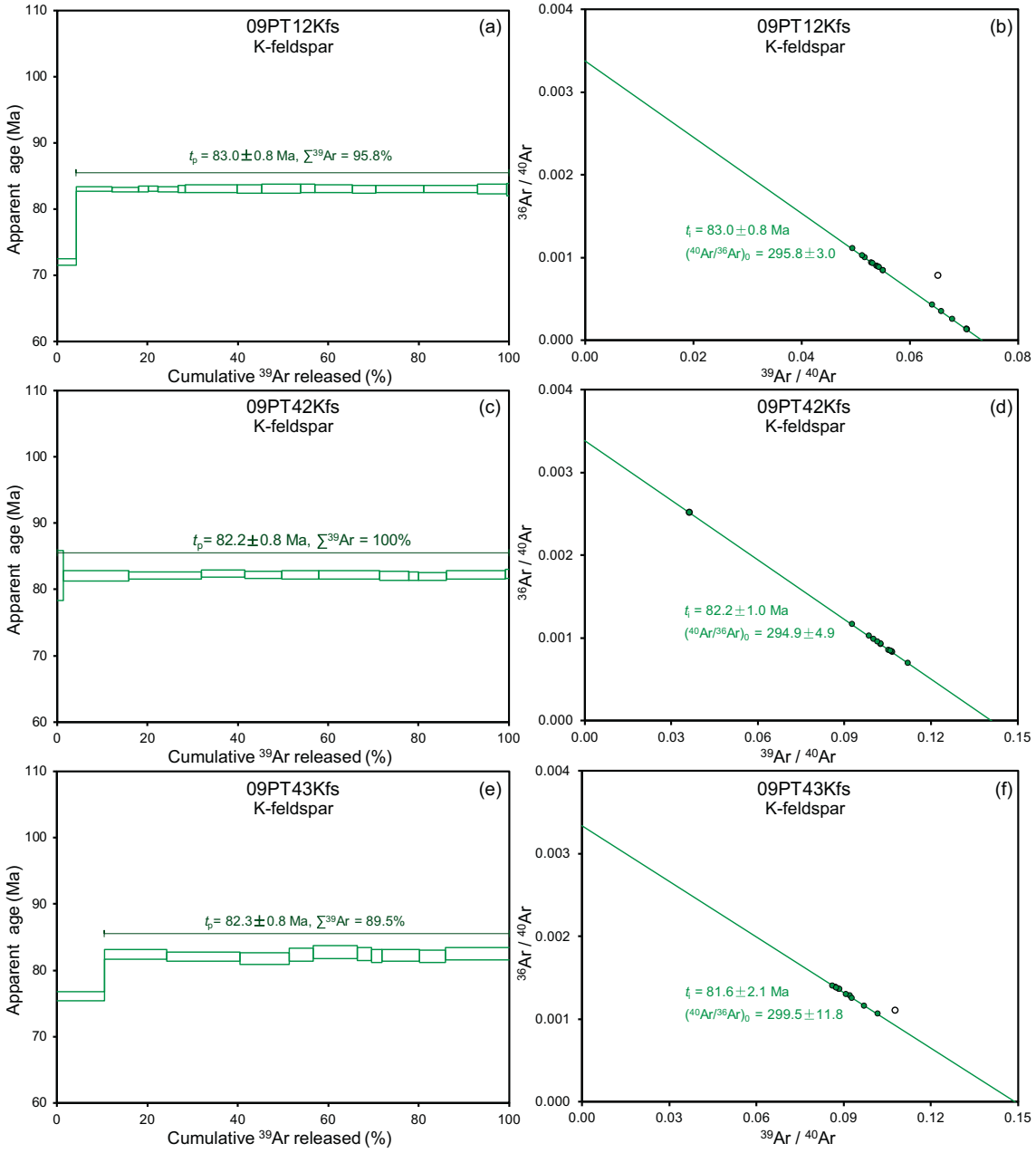

Fig. 6. Plots of ^{40}Ar/^{39}Ar age spectra and inverse isochrons of K-feldspars 09PT12Kfs, 09PT42Kfs and 09PT43Kfs by laser stepwise heating.

step 24. Here it is worth noting that a flat age section is obtained for steps 10 to 13 with a weighted mean age of 157.0 ± 1.7 Ma covering 34.56% ^{39}Ar, is consistent with the ^{40}Ar/^{39}Ar age of the coexisting muscovite 09NL05Ms.

On the inverse isochron diagram of ^{36}Ar/^{40}Ar vs. ^{39}Ar/^{40}Ar, the distribution of data points show very regularly as the arrows in Fig. 7b. These points obviously distribute in three groups and well define two "isochron" lines. The first two steps (Group I) are close to the ^{36}Ar/^{40}Ar axis with very low ^{39}Ar/^{40}Ar ratios, representing excess ^{40}Ar with ^{40}Ar/^{36}Ar ratios of 543 and 633. The data points of steps 3–9 (Group II) yield an isochron line with age of 137.0 ± 2.2 Ma (MSWD = 2.9, green points and line) corresponding to an initial ^{40}Ar/^{36}Ar ratio of 689.8 ± 11.4, much higher than the ratio of the modern atmosphere. If applying the initial ratio to exclude the non-radiogenic argon, the ages of steps 4–9 are corrected to 149.8, 139.8, 137.7, 135.8, 138.4 and 136.4 Ma respectively with a weighted mean age of 137.0 ± 1.7 Ma (Fig. 7a, green dash line). This isochron age and weighted mean age are well concordant with the age of sericite 09NL01Ser by ^{40}Ar/^{39}Ar laser stepwise heating (Fig. 5), indicating the postmineralization fluid overprinting.

On the other hand, the data points of steps 10–24 (Group III) define another "isochron" line with age of 160.7 ± 1.7 Ma (MSWD = 0.7) (Fig. 7b, blue points and line), corresponding to an initial ^{40}Ar/^{36}Ar ratio of 257.0 ± 3.0, which is much lower than the modern atmospheric ratio of 295.5. By applying the ratio of 257.0 to exclude non-radiogenic ^{40}Ar, a flat plateau of 160.7 ± 1.6 Ma (Σ^{39}Ar = 57.4%) is obtained (Fig. 7a, blue dash lines). The "plateau" and "isochron" ages for the final steps (10–24) are consistent with that of paragenetic muscovite 09NL05Ms within analysis errors, representing the mineralization time. These "isochron" lines will be further discussed in the section of "Discussion".

4.2.3.2. 09PT37Q. The sample was crushed in 28 steps with total of 23,590 pestle drops. A declining age spectrum is obtained from the

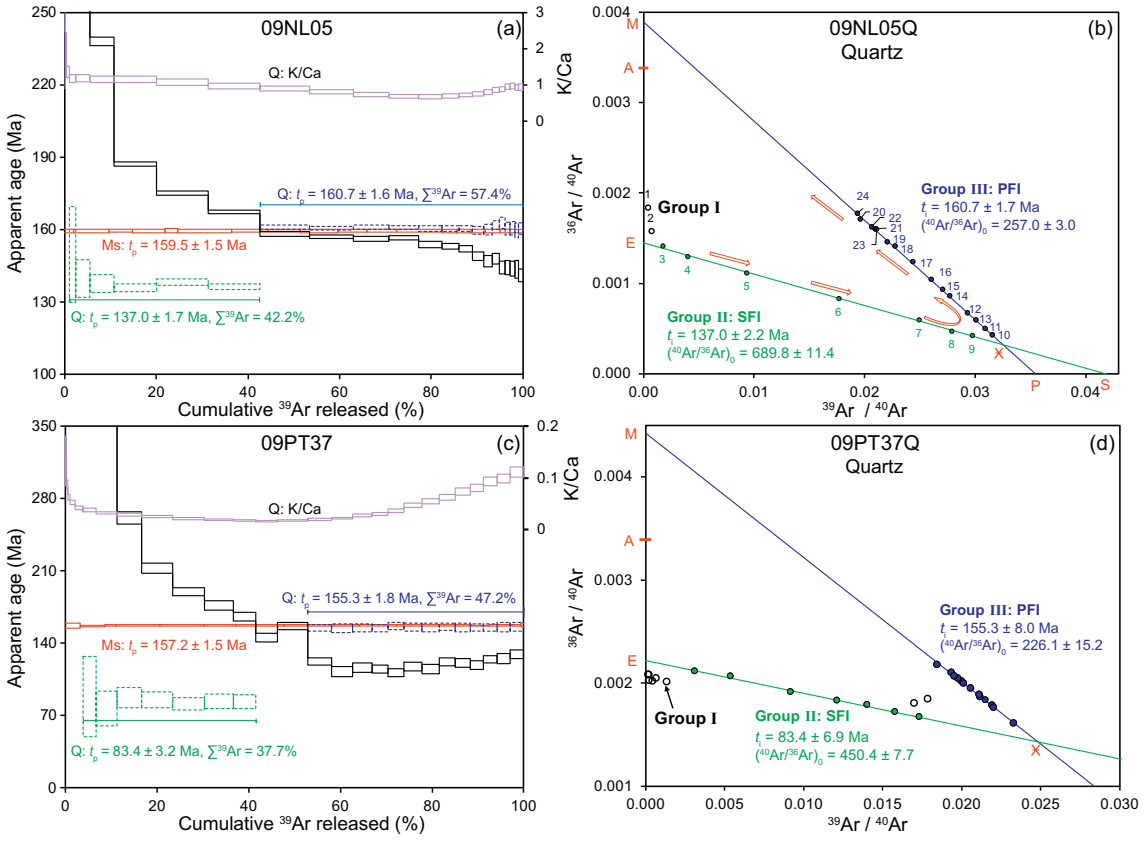

Fig. 7. Plots of age and K/Ca spectra and inverse isochrons of quartz samples 09NL05Q (a & b) and 09PT37Q (c & d) by progressive crushing. (a) The black, blue and green lines are obtained by excluding non-radiogenic ^{40}Ar with 295.5, 257.0, and 689.8; (b) A – modern atmosphere. P and S represent the radiogenic components (i.e. $^{39}Ar_K/^{40}Ar^*$ ratios, corresponding to the apparent ages) of the primary (or muscovite) and secondary fluid inclusions (K-feldspar or sericite) respectively. E – excess ^{40}Ar. The red arrows show the trend of data point distribution as the crushing procedure progresses. PFI and SFI are abbreviations for the primary and secondary fluid inclusions, respectively. The data points are preliminarily attributed to three groups I, II and III, corresponding to excess ^{40}Ar, SFIs and PFIs respectively. (For interpretation of the references to colour in this figure legend, the reader is referred to the web version of this article.)

experiment data (Fig. 7c, the dark solid line), marked with abnormally old apparent ages of 3862 Ma at the first steps, decreasing dramatically to 261.2 Ma at step 9, then declining gradually to 122.5 Ma at step 16. A plateau is yielded for steps 17–22 with an age of 114.7 ± 2.2 Ma, followed by slightly increasing apparent ages in the last 8 steps, up to 129.5 Ma at the end.

On the inverse isochron diagram of $^{36}Ar/^{40}Ar$ vs. $^{39}Ar/^{40}Ar$, the crushing data points also distribute in three groups and form two well-defined isochron lines (Fig. 7d). The crushing data points of the first six steps (Group I) are close to the $^{36}Ar/^{40}Ar$ axis with very low $^{39}Ar/^{40}Ar$ ratios, representing excess ^{40}Ar with $^{40}Ar/^{36}Ar$ ratios of 480 to 497. The data points of steps 7–13 (Group II) define an isochron line with age of 83.4 ± 6.9 Ma (MSWD = 0.4) (Fig. 7d, green points and line) corresponding to an initial $^{40}Ar/^{36}Ar$ ratio of 450.4 ± 7.7, much higher than the ratio of the modern atmosphere, which is usually attributed to the excess ^{40}Ar in these steps. If this initial $^{40}Ar/^{36}Ar$ ratio is applied to correct the non-radiogenic argon, the ages of the 7–13 steps are 88.4, 76.9, 87.3, 85.1, 81.2, 83.9 and 83.2 Ma, with a weighted mean age of 83.4 ± 3.2 Ma and Σ^{39}Ar = 37.7% (Fig. 7c, green dash line). The isochron age and weighted mean age are concordant with the ages of K-feldspar samples by $^{40}Ar/^{39}Ar$ laser heating (Fig. 6).

The last thirteen steps (Group III) yield a well-defined isochron line with age of 155.3 ± 8.0 Ma (MSWD = 0.1) (Fig. 7d, blue points and line), corresponding to initial $^{40}Ar/^{36}Ar$ ratio of 226.1 ± 15.2, much lower than the modern atmospheric ratio of 295.5. If applying this initial $^{40}Ar/^{36}Ar$ ratio to exclude the non-radiogenic ^{40}Ar for the final steps, a flat plateau of 155.3 ± 1.8 Ma (Σ^{39}Ar = 47.2%) is obtained (Fig. 7c, blue dash lines). The "plateau" and "isochron" ages for the final steps are in agreement with the age of paragenetic muscovite 09PT37Ms within analysis errors (Fig. 4c, d), representing the timing of tungsten mineralization.

5. Discussion

5.1. Mineralization ages

Many tin-tungsten ore deposits in southern Jiangxi Province have been determined by ore muscovite $^{40}Ar/^{39}Ar$ dating, molybdenite Re–Os dating and metallogenic granite zircon U–Pb dating, indicating that tin-tungsten mineralization occurred ca. 160–150 Ma (Mao et al., 2011; Mao et al., 2008). In Piaotang, the granitic zircon U–Pb ages are 162–160 Ma (He et al., 2010; Zhang et al., 2017; Zhang et al., 2009), molybdenite Re–Os isochron age 155 Ma (Zhang et al., 2009), LA-ICP-MS cassiterite U–Pb mean age 159.5 ± 1.5 Ma (Zhang et al., 2017), and muscovite, cassiterite, wolframite and quartz $^{40}Ar/^{39}Ar$ ages ranging from 160 to 153 Ma (Bai et al., 2018; this study; Bai et al., 2013). All the isotopic geochronological data are concordant, indicating that the tin-tungsten mineralization followed the granite intrusion.

The hydrothermal mineral $^{40}Ar/^{39}Ar$ dates should be interpreted as crystalisation ages rather than cooling ones. The main reasons are listed for muscovite as follows:

(1) When the magma-related ore-bearing hydrothermal fluid transported along tectonic fractures into the cool surrounding rocks, the fluid cooled down quickly to the mineral closure temperatures and formed the ore veins in a short period. The muscovite ages of 160–153 Ma (Bai, 2014) were probably recorded the pulsation of fluid activities during mineralization.

(2) All the muscovite $^{40}Ar/^{39}Ar$ age spectra are perfectly flat from the tungsten deposits in the South China (Fig. 4; Bai, 2014; Bai et al., 2013), not showing a zone of partial accumulation of radiogenic ^{40}Ar.
(3) These new geochronological dates are well concordant within analysis errors: granite zircon U–Pb mean age of 159.8 ± 0.3 Ma, hydrothermal cassiterite U–Pb mean age of 159.5 ± 1.5 Ma (Zhang et al., 2017), paragenetic cassiterite and muscovite $^{40}Ar/^{39}Ar$ isochron ages of 158.6 ± 1.4 Ma and 159.3 ± 0.8 Ma respectively (Bai et al., 2013).

5.2. Argon reservoirs and release patterns

Qiu and Wijbrans (2008) summarized the argon reservoirs of the ultra-high pressure (UHP) metamorphic eclogitic garnets released by progressive crushing (Fig. 7b of Qiu and Wijbrans, 2008): "(I) First steps, excess ^{40}Ar ($^{40}Ar_{ex}$) trapped in secondary fluid inclusions which distribute along cracks and are more easily extracted by crushing. $^{40}Ar/^{39}Ar$ isochron of secondary fluid inclusions could be obtained occasionally (Qiu and Jiang, 2007). (II) Middle steps, mixture from secondary and primary fluid inclusions. (III) Final steps, mixture of radiogenic ($^{40}Ar_R$) and trapped argon in small primary fluid inclusions and atmospheric argon (Air) from the crusher". In those cases, the argon reservoirs include the SFIs, the PFIs and the crusher air. The argon components contain in situ potassium decay radiogenic $^{40}Ar_R$, parentless excess $^{40}Ar_{ex}$, and the modern atmospheric argon.

The first time that hydrothermal sphalerites from the Fankou Pb-Zn Deposit were analysed by progressive crushing, results indicated two isochron lines, which were interpreted as the SFI and PFI isochron lines (Qiu and Jiang, 2007), and were subsequently verified further by the correlation plots of K-Cl-Ar (Jiang et al., 2012). Some sphalerites were shown to contain K-rich microlites. The crushed powder by $^{40}Ar/^{39}Ar$ furnace heating yielded indistinguishable ages from the PFIs (Qiu and Jiang, 2007), indicating another argon reservoir from the K-rich microlites, which were formed during the sphalerite crystallization and yielded the same $^{40}Ar/^{39}Ar$ isochron line. Jiang et al. (2012) sorted the argon release patterns into four cases based on K concentrations (Fig. 9b of Jiang et al., 2012).

For the granite-associated W-Sn deposits in the South Jiangxi, the post-mineralization K-feldspar becomes another new argon reservoir, causing the wolframite and quartz samples to yield more complicated $^{40}Ar/^{39}Ar$ age spectra. Progressive crushing releases argon in a sequence: initially from the secondary fluid inclusions, then the primary fluid inclusions and finally from the K-bearing minerals. We proposed a gas mixing release pattern for the wolframite 09PT37Wlf by crushing (Fig. 9 of Bai et al., 2013). Now we discuss the isochron or gas mixing lines on the inverse isochron diagram of $^{36}Ar/^{40}Ar$ vs $^{39}Ar/^{40}Ar$ in another way to provide further information on the timing of mineralization.

5.3. Isochron diagrams and gas mixing lines

Inverse isochron diagram is used more often than the normal one. We will discuss the isochron and gas mixing lines on the inverse isochron plot in detail, and then on the normal one briefly.

5.3.1. Inverse isochron

In order to better comprehend the gas mixing lines, here we briefly review the inverse isochron plot (Fig. 8a) of $^{36}Ar/^{40}Ar$ (Y-axis) vs. $^{39}Ar/^{40}Ar$ (X-axis) (Kuiper, 2002; McDougall and Harrison, 1999; Roddick et al., 1980; Turner, 1971). The two intercepts correspond to the pure trapped and pure radiogenic components in the sample (McDougall and Harrison, 1999). The *x* intercept of the isochron line, the reverse $^{40}Ar/^{39}Ar$ ratio, is used for age calculation with the equation:

$$t = \frac{1}{\lambda}\ln\left(1 + J\frac{^{40}Ar_R}{^{39}Ar_K}\right)$$

For a given *J* value, the ages progress inversely from old to young along the X-axis. The data points on the right side of the isochron line may indicate partial argon loss or contamination from younger minerals.

The *y* intercept (the reverse $^{40}Ar/^{36}Ar$ ratio) represents the trapped argon composition and the air component (i.e., released from the crusher). An intercept below "Air" indicates that some parentless excess ^{40}Ar ($^{40}Ar_{ex}$) was trapped during crystallization.

The potential drawbacks and limitations of the normal isochron plot and the advantages of the inverse isochron plot are described in detail by McDougall and Harrison (1999). The argon reservoirs or end-members, such as the air, parentless excess ^{40}Ar, and radiogenic ^{40}Ar of the old PFIs and young SFIs, are showed clearly on the inverse isochron plot, which help us understand the isochron and gas mixing lines.

We'll discuss the $^{40}Ar/^{39}Ar$ isochron or mixing lines, according to the argon release sequence from the different reservoirs by progressive crushing, in the following sections.

5.3.2. SFI isochron line

The SFI gases released in the first crushing steps contain excess ^{40}Ar (close to point E in Fig. 8b) and yield abnormally old apparent ages. Usually the SFI gases are mixed with the PFI gases, causing the data points to move from SFI to PFI along a curve (Qiu and Wijbrans, 2006; Qiu and Wijbrans, 2008). These points should locate within triangle AEX (Fig. 8b), or left of the PFI isochron line AX. In practice, it seems that SFIs always contain excess ^{40}Ar, such as the UHP metamorphic eclogitic garnets from Dabieshan (Qiu and Wijbrans, 2006; Qiu and Wijbrans, 2008), the sphalerites from the Fankou Pb-Zn Deposit (Jiang et al., 2012; Qiu and Jiang, 2007) and the cassiterite, wolframites and quartzs from the southern China tin-tungsten deposits (Bai et al., 2013, this study).

It is not easy to obtain an SFI isochron line. To increase chances, one should focus on SFIs with high K concentration and extract gas from them by gentle crushing, which allows for sample grains to be broken along microcracks to target gas release from SFIs and avoid PFIs. This can allow for an SFI isochron line to be obtained in the first steps (lines EX in Fig. 7b, Fig. 7d and Fig. 8b). At this moment, the line EX is simply interpreted as a SFI isochron, because the exact initial $^{40}Ar/^{36}Ar$ ratio trapped in SFIs is unknown.

SFI isochron lines have been rarely obtained and difficultly verified by other methods. This is the first report that the SFI isochron ages of quartz samples by crushing are directly confirmed by the K-rich minerals of sericite and K-feldspar with the $^{40}Ar/^{39}Ar$ laser heating technique, though the K-Cl-Ar correlation diagrams have been probably applied to obtain the SFI ages (Bai et al., 2013; Jiang et al., 2012).

5.3.3. PFI isochron line

After the SFIs have been exhausted in the first steps, in cases of sufficient high potassium inside the PFIs, a PFI isochron line (PA in Fig. 8b) can be obtained. This uses gas from the final crushing steps because the most PFIs are isolated and small (ca. 1 to 5 μm). Many PFI isochron lines have been reported previously (Jiang et al., 2012; Qiu and Jiang, 2007; Qiu and Wijbrans, 2006, 2008). The cassiterite 09PT01Cst from Piaotang is a good example of a PFI isochron (Fig. 4B of Bai et al., 2013). It should be mentioned here that the data points of PFIs are distributed in a trend from X to A (air) because the air released from the crusher becomes more dominant due to the very fine grain sizes and the high number (several hundreds) of pestle drops during late-stage crushing analyses.

5.3.4. Gas mixing lines

After several thousand pestle drops during crushing, powder sizes reach as sub-micron scale (Bai et al., 2013). Prolonged crushing will

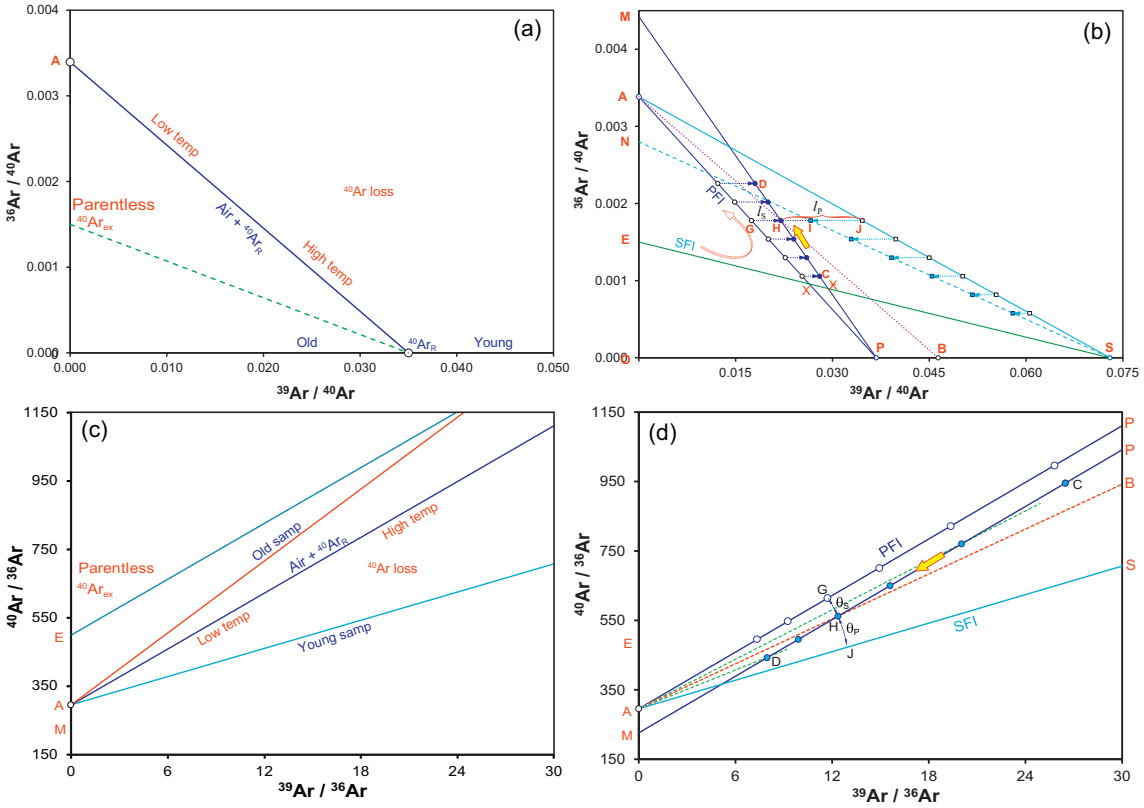

Fig. 8. (a) The inverse isochron; (b) Gas mixing lines of hydrothermal non-potassium minerals based on the data of quartz 09PT37Q by $^{40}Ar/^{39}Ar$ progressive crushing. A – modern atmosphere. P and S represent the radiogenic components of the PFIs (or muscovite) and SFIs (K-feldspar or sericite) respectively. E – parentless excess ^{40}Ar. The red arrows show the trend of data point distribution as the crushing procedure progresses. EX – the SFI isochron line containing excess ^{40}Ar. PA – the PFI isochron line. SA – $^{40}Ar_{ex}$-free SFI isochron line, or isochron line of post-mineralization K-feldspar and sericite. PM – gas mixing line of PFIs and $^{40}Ar_{ex}$-free SFIs, corresponding to the PFI age and a low initial $^{40}Ar/^{36}Ar$ ratio. SN – a potential gas mixing line by dominant post-mineralization components with minor residual PFIs. BA – an impossible gas mixing line with a constant PFI/SFI proportion. (For interpretation of the references to colour in this figure legend, the reader is referred to the web version of this article.)

cause the K-rich microcrystals within quartz grains (such as mica and K-feldspar) to release gases. In this study, two quartz samples do contain mica or/and K-feldspar microcrystals (Fig. 3). Below we discuss the crystal structures of mica and K-feldspar and their likelihoods of releasing argon by prolonging crushing.

The mica group belongs to phyllosilicates in which the basic unit is composed of sheets of $(Si,Al)O_4$ tetrahedra (N_{Si}:N_{Al} = 3:1) cross-linked with sheets of $(Al,Mg,Fe)(O,OH)_6$ octahedra (Fig. 9a). The cross-linked double layer is bound firmly and has a negative charge. The charge is balanced by singly charged large cations (e.g., K^+ in muscovite) that join the crosslinked double layers to form the complete structure. This structure enables (001) perfect cleavage, along which K is exposed and released easily.

The K-feldspar belongs to tektosilicates (Fig. 9b). The crystal structure of feldspar consists of a continuous, negatively charged, three-dimensional framework made up of corner-sharing SiO_4 and AlO_4 tetrahedra and positively charged cations (K^+) that occupy relatively large interstices within the framework. This structure enables (001) and (010) perfect cleavages, along which K is exposed and released easily.

In the crushing process, muscovite and orthoclase are broken preferentially along cleavages that facilitate the exposure of K^+, representing the release of both irradiated $^{39}Ar_K$ from ^{39}K and radiogenic $^{40}Ar_R$ from in situ decay of ^{40}K. It is noted that K may not be released from muscovite when the crushing force is perpendicular to (001), whereas K can be released from orthoclase in any case as it has two sets of cleavages. Therefore, K-feldspar releases argon more readily than muscovite by crushing.

Now we will discuss palaeoatmospheric $^{40}Ar/^{36}Ar$ ratios. Cadogan (1977) provided the determination of a palaeoatmospheric $^{40}Ar/^{36}Ar$ ratio of 291.0 ± 1.5 for the 380 Ma atmospheric argon dissolved in the Rynie chert in Scotland. Turner (1988) obtained the palaeoatmospheric $^{40}Ar/^{36}Ar$ ratios of 280–297 for the 1700 Ma Gunflint chert using four procedures by stepped heating. Compared with the above data, the initial $^{40}Ar/^{36}Ar$ ratio of 268.3 ± 1.7 of the 157 Ma wolframite 09PT37Wlf (Fig. 4G & H of Bai et al., 2013) seemed much lower than expected. In order to explain the low initial ratio and declining age spectrum of the final crushing steps, we presented a gas mixing pattern (Fig. 9 of Bai et al., 2013). According to the pattern, a given data point is considered as a mixture of an atmospheric and a radiogenic component, and the latter can be further recognized as a radiogenic argon mixture with different proportions of the PFI (muscovite) and SFI (K-feldspar). The pattern helps us understand the gas mixing line.

In this study, the quartz samples 09NL05Q and 09PT37Q analysed by crushing also yield similar declining age spectra and low initial $^{40}Ar/^{36}Ar$ ratios. Now we present the mixing line PM in another way as shown in Fig. 8b. Because of the contributions of secondary products of post-mineralization fluids (or secondary components, point S), such as sericite, K-feldspar and very fine liquid SFIs without excess ^{40}Ar, the data points of PFI isochron line (PA) move to mixing line (PM), i.e., from point G to point H. The radiogenic component contribution of the PFIs to the SFIs can be calculated: $^{BS}/_{PB} = {}^{HJ}/_{GH} = {}^{l_P}/_{l_S}$. As the crushing procedure progresses, the proportions of secondary components and crusher air increase, and the data points distribute along line PM from point C toward point D. The open red arrow shows the shifting trend of the gas mixing data points in Fig. 8b. Therefore, the data points of the secondary components (as minor) mix with the primary components (as dominant) by the progressive crushing technique. This result in a mixing line PM, whose intercept on the X-axis (point P) has the same point as the primary components, corresponding to the PFI age. The Y-axis intercept moves from point A (atmosphere) to point M,

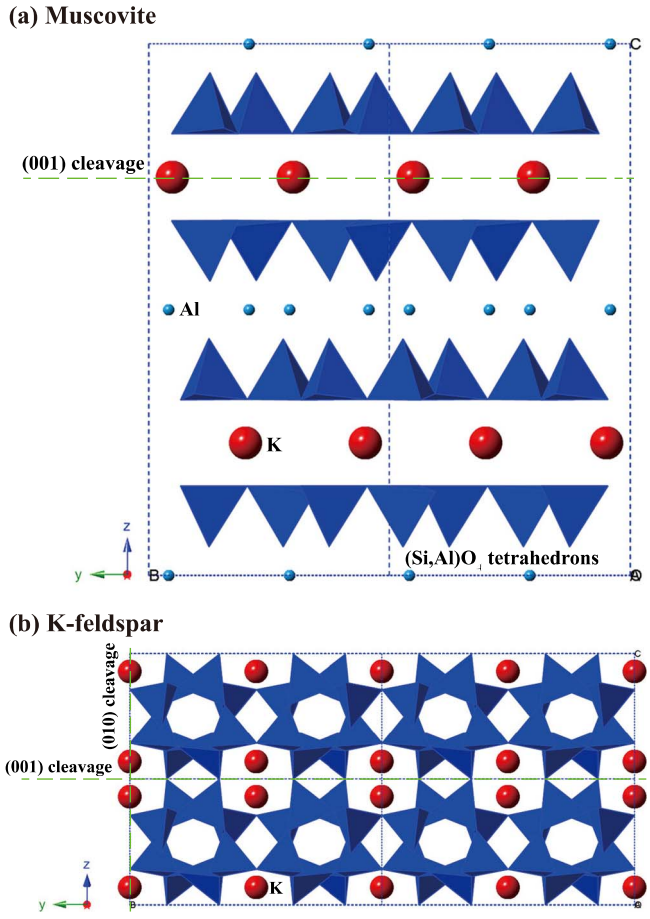

Fig. 9. (a) The crystal structures of muscovite-2M1 viewed along the a-axis, based on the data of Güven (1971). (b) The crystal structure of orthoclase viewed along the a-axis, based on the data of Prince et al. (1973).

corresponding to a $^{40}Ar/^{36}Ar$ initial ratio lower than 295.5. Quartz sample 09NL05Q contains only sericite microcrystals and thus yields a monotonically decreasing age spectrum in the final crushing steps (Fig. 7a). However, quartz sample 09PT37Q contains both K-feldspar and muscovite microcrystals. Because of the crystal structure differences (Fig. 9), argon is more readily released from the young K-feldspar (82.5 Ma) than the older muscovite (157.2 Ma) by crushing, resulting in apparent ages that have minima in the middle steps and increase slightly in the final steps (Fig. 7c, dark lines). On the other hand, the K/Ca ratios of 09PT37Q in the final crushing steps are gradually rising up (Fig. 7c, purple lines), indicating gas release from a K-rich phase. Therefore, the gas mixing line is reasonable. These gas mixing data points should be within the triangle AXS area.

On the other hand, if the $^{40}Ar_{ex}$-free secondary components are dominant, a gas mixing line SN corresponding to the SFI age with an initial $^{40}Ar/^{36}Ar$ ratio slightly larger than 295.5, may be theoretically obtained (Fig. 8b). It seems impossible to yield a gas mixing line BA by progressive crushing, along which all the data points keep the constant proportion of primary and secondary components and correspond to an intermediate age between primary and secondary fluid inclusions.

These patterns could not be interpreted clearly by previous gas mixing models (Bai et al., 2013). This new model (Fig. 8b) yields more information than previous models and will both help us understand the $^{40}Ar/^{39}Ar$ dating results and be used for reference by other isotopic mixing isochron systems.

5.3.5. Normal isochron and gas mixing lines

The normal isochron plot of $^{40}Ar/^{36}Ar$ vs $^{39}Ar/^{36}Ar$ (Fig. 8c) is less used than the inverse one now. The isochron age is based on the line slope of the $^{40}Ar_R/^{39}Ar$ ratio. The Y intercept represents the initial $^{40}Ar/^{36}Ar$ ratio of the trapped argon: A – the modern atmospheric argon; E – the trapped parentless excess argon ($^{40}Ar_{ex}$); M – the initial $^{40}Ar/^{36}Ar$ ratio lower than the modern atmospheric argon, probably expressing the trapped ancient atmospheric argon or a gas-mixing intercept as shown in the cases of this study.

Now we explain for the gas mixing line PM on the normal isochron plot Fig. 8d. Line AP′ is the isochron line of the muscovite or the primary fluid inclusions, and line AS is that of the K-feldspar or the secondary fluid inclusions with the intercepts of modern atmospheric argon. Line PM is the gas mixing line of the PFIs and SFIs, parallel to the line AP′ with initial $^{40}Ar/^{36}Ar$ ratio lower than 298.56 (Lee et al., 2006). The radiogenic component contribution of the PFIs to SFIs in a step can be calculated by the ratio of $^{\theta_P}/_{\theta_S}$, well concordant with the ratio of $^{l_P}/_{l_S}$ in Fig. 8b.

6. Conclusion

Some important points are obtained from this study:

1) The muscovites from the Niuling and Piaotang tungsten ores by $^{40}Ar/^{39}Ar$ laser stepwise heating yield very flat age spectra with ages of 160 and 157 Ma, well-constraining that the mineralization occurred in late Jurassic. The $^{40}Ar/^{39}Ar$ ages of Niuling sericite (137 Ma) and Piaotang K-feldspar veins (83 Ma) cutting the ore bodies indicate the post-mineralization hydrothermal activities in the mining areas took place in early and late Cretaceous.
2) Two quartz samples from the tungsten ores, which underwent post-mineralization fluid overprinting, were analysed by $^{40}Ar/^{39}Ar$ progressive crushing and yield two regression lines on inverse isochron diagrams, corresponding respectively to the ages of secondary fluid inclusions (the first line) and primary fluid inclusions (the second line). The quartz 09NL05Q from Niuling yields a SFI age of 137 Ma concordant with the sericite 09NL01Ser age, and a PFI age of 161 Ma in agreement with the paragenetic muscovite 09NL05Ms age. The quartz 09PT37Q from Piaotang yields a SFI age of 83 consistent with the K-feldspar vein age, and a PFI age of 155 Ma in agreement with the paragenetic muscovite 09NL05Ms age, all within analytical errors. This is the first time that SFI ages are directly verified by ages from coexisting K-rich phases (sericite and K-feldspar).
3) Abnormally low initial $^{40}Ar/^{36}Ar$ ratios of 257 and 226 are obtained from the second regression lines of 09NL05Q and 09PT37Q respectively, much lower than the ratio of modern atmosphere. Gas mixing lines are proposed where the data points of the second lines indicate mixing between the PFIs (or muscovite formed during mineralization) and the $^{40}Ar_{ex}$-free SFIs (or sericite and K-feldspar formed in post-mineralization), demonstrating that lines corresponding to the PFI ages have low initial $^{40}Ar/^{36}Ar$ ratios. An intermediate age between PFI and SFI ages might not be yielded, because the progressive crushing technique cannot release gases with a constant PFI/SFI proportion. Therefore, the gas mixing lines can obtain meaningful geological ages. The $^{40}Ar/^{39}Ar$ progressive crushing technique is thus very useful to determine the timing of geofluid activity. The new gas mixing model releases abundant information, which will help us better understand the $^{40}Ar/^{39}Ar$ dating results.

Supplementary data to this article can be found online at https://doi.org/10.1016/j.chemgeo.2018.02.039.

Acknowledgments

We acknowledge the contribution of Donald Dingwell, Leah E.

Morgan and two anonymous reviewers. We thank Shuiyuan Yang for his kind helps with the EMPA, Kehao Lu and Jinlong Fang for fieldwork. This study was financially supported by the Natural Science Foundation of China (No.41503053, No.41630315 & No.41688103) and the National Basic Research Program of China (No.2012CB416706). A 100 Talents Program of the Chinese Academy of Sciences to Yingde Jiang is also acknowledged.

References

Bai, X.J., 2014. Mineralization Ages of the Tungsten Deposits in Southern Jiangxi Province: New Insights from $^{40}Ar/^{39}Ar$ Progressive Crushing. Doctoral Dissertation of the China Universityof Geosciences, Wuhan, China (129 pp).

Bai, X.J., Wang, M., Jiang, Y.D., Qiu, H.N., 2013. Direct dating of tin–tungsten mineralization of the Piaotang tungsten deposit, South China, by $^{40}Ar/^{39}Ar$ progressive crushing. Geochim. Cosmochim. Acta 114, 1–12.

Bai, X.J., Qiu, H.N., Liu, W.G., Mei, L.F., 2018. Automatic $^{40}Ar/^{39}Ar$ dating techniques using multicollector ARGUS VI noble gas mass spectrometer with self-made peripheral apparatus. J. Earth Sci. 29 (2). http://dx.doi.org/10.1007/s12583-017-0948-9.

Cadogan, P.H., 1977. Palaeoatmospheric argon in Rhynie chert. Nature 268, 38–41.

Güven, N., 1971. The crystal structures of 2M1 phengite and 2M1 muscovite. Z. Krist. 134 (3–4), 196–212.

He, Z.Y., Xu, X.S., Zou, H.B., Wang, X.D., Yu, Y., 2010. Geochronology, petrogenesis and metallogeny of Piaotang granitoids in the tungsten deposit region of South China. Geochem. J. 44 (4), 299–313.

Jiang, Y.D., Qiu, H.N., Xu, Y.G., 2012. Hydrothermal fluids, argon isotopes and mineralization ages of the Fankou Pb-Zn deposit in south China: insights from sphalerite $^{40}Ar/^{39}Ar$ progressive crushing. Geochim. Cosmochim. Acta 84, 369–379.

Kelley, S., Turner, G., Butterfield, A.W., Shepherd, T.J., 1986. The source and significance of argon isotopes in fluid inclusions from areas of mineralization. Earth Planet. Sci. Lett. 79 (3–4), 303–318.

Kendrick, M.A., Phillips, D., 2009. New constraints on the release of noble gases during in vacuo crushing and application to scapolite Br-Cl-I and $^{40}Ar/^{39}Ar$ age determinations. Geochim. Cosmochim. Acta 73 (19), 5673–5692.

Kendrick, M.A., Burgess, R., Pattrick, R.A.D., Turner, P.G., 2001. Halogen and Ar–Ar age determinations of inclusions within quartz veins from porphyry copper deposits using complementary noble gas extraction techniques. Chem. Geol. 177 (3–4), 351–370.

Koppers, A.A.P., 2002. ArArCALC - software for $^{40}Ar/^{39}Ar$ age calculations. Comput. Geosci. 28 (5), 605–619.

Kuiper, Y.D., 2002. The interpretation of inverse isochron diagrams in $^{40}Ar/^{39}Ar$ geochronology. Earth Planet. Sci. Lett. 203 (1), 499–506.

Lee, J.Y., Marti, K., Severinghaus, J.P., Kawamura, K., Yoo, H.S., Lee, J.B., Kim, J.S., 2006. A redetermination of the isotopic abundances of atmospheric Ar. Geochim. Cosmochim. Acta 70 (17), 4507–4512.

Li, B., 2011. Synchronization theory and tungsten-polymetallic mineralization distribution in the Qianlishan-Qitianling area, southern Hunan. J. Earth Sci. 22 (6), 726–736.

Liu, N., Yu, C., 2011. Analysis of onset and development of ore formation in Dajishan tungsten ore area, Jiangxi Province, China. J. Earth Sci. 22 (1), 67–74.

Liu, Z.Q., Mei, L.F., Qiu, H.N., Bo, S.C., Tang, J.G., Yun, J.B., 2011. $^{40}Ar/^{39}Ar$ geochronology constraints on hydrocarbon accumulation and destruction periods in the Bankeng paleo-reservoir in the southern margin of the middle Yangtze block. Chin. Sci. Bull. 56 (26), 2803–2812.

Liu, Y., Cheng, Q., Xia, Q., Wang, X., 2014. Mineral potential mapping for tungsten polymetallie deposits in the Nanling Metallogenic Belt, South China. J. Earth Sci. 25 (4), 689–700.

Mao, J.W., Xie, G.Q., Guo, C.L., Yuan, S.D., Cheng, Y.B., Chen, Y.C., 2008. Spatial-temporal distribution of Mesozoic ore deposits in South China and their metallogenic settings. Geol. J. China Univ. 14 (4), 510–526.

Mao, J.W., Chen, M.H., Yuan, S.D., Guo, C.L., 2011. Geological characteristics of the Qinhang (or Shihang) Metallogenic Belt in South China and spatial-temporal distribution regularity of mineral deposits. Acta Geol. Sin. 85 (5), 636–658.

McDougall, I., Harrison, T.M., 1999. Geochronology and Thermochronology by the $^{40}Ar/^{39}Ar$ Method. Oxford University Press, Oxford, New York (269 pp).

Phillips, D., Miller, J.M., 2006. $^{40}Ar/^{39}Ar$ dating of mica-bearing pyrite from thermally overprinted Archean gold deposits. Geology 34 (5), 397–400.

Prince, E., Donnay, G., Martin, R.F., 1973. Neutron diffraction refinement of an ordered orthoclase structure. Am. Mineral. 58 (5–6), 500–507.

Qiu, H.N., 1996. $^{40}Ar–^{39}Ar$ dating of the quartz samples from two mineral deposits in western Yunnan (SW China) by crushing in vacuum. Chem. Geol. Isot. Geosci. 127 (1–3), 211–222.

Qiu, H.N., Dai, T.M., 1989. $^{40}Ar/^{39}Ar$ technique for dating the fluid inclusions of quartz from a hydrothermal deposit. Chin. Sci. Bull. 34 (22), 1887–1890.

Qiu, H.N., Jiang, Y.D., 2007. Sphalerite $^{40}Ar/^{39}Ar$ progressive crushing and stepwise heating techniques. Earth Planet. Sci. Lett. 256 (1–2), 224–232.

Qiu, H.N., Wijbrans, J.R., 2006. Paleozoic ages and excess ^{40}Ar in garnets from the Bixiling eclogite in Dabieshan, China: new insights from $^{40}Ar/^{39}Ar$ dating by stepwise crushing. Geochim. Cosmochim. Acta 70 (9), 2354–2370.

Qiu, H.N., Wijbrans, J.R., 2008. The Paleozoic metamorphic history of the Central Orogenic Belt of China from $^{40}Ar/^{39}Ar$ geochronology of eclogite garnet fluid inclusions. Earth Planet. Sci. Lett. 268 (3–4), 501–514.

Qiu, H.N., Zhu, B.Q., Sun, D.Z., 2002. Age significance interpreted from $^{40}Ar–^{39}Ar$ dating of quartz samples from the Dongchuan Copper Deposits, Yunnan, SW China, by crushing and heating. Geochem. J. 36 (5), 475–491.

Qiu, H.N., Wijbrans, J.R., Brouwer, F.M., Yun, J.B., Zhao, L.H., Xu, Y.G., 2010. Amphibolite facies retrograde metamorphism of the Zhujiachong eclogite, SE Dabieshan: $^{40}Ar/^{39}Ar$ age constraints from argon extraction using UV-laser microprobe, in vacuo crushing and stepwise heating. J. Metamorph. Geol. 28 (5), 477–487.

Qiu, H.N., Wu, H.Y., Yun, J.B., Feng, Z.H., Xu, Y.G., Mei, L.F., Wijbrans, J.R., 2011. High-precision $^{40}Ar/^{39}Ar$ age of the gas emplacement into the Songliao Basin. Geology 39 (5), 451–454.

Roddick, J.C., Cliff, R.A., Rex, D.C., 1980. The evolution of excess argon in alpine biotites — a $^{40}Ar–^{39}Ar$ analysis. Earth Planet. Sci. Lett. 48 (1), 185–208.

Shepherd, T.J., Darbyshire, D.P.F., 1981. Fluid inclusion Rb–Sr isochrons for dating mineral deposits. Nature 290 (5807), 578–579.

Turner, G., 1971. $^{40}Ar–^{39}Ar$ ages from the lunar maria. Earth Planet. Sci. Lett. 11 (1–5), 169–191.

Turner, G., 1988. Hydrothermal fluids and argon isotopes in quartz veins and cherts. Geochim. Cosmochim. Acta 52 (6), 1443–1448.

Turner, G., Bannon, M.P., 1992. Argon isotope geochemistry of inclusion fluids from granite-associated mineral veins in southwest and northeast England. Geochim. Cosmochim. Acta 56 (1), 227–243.

Turner, G., Wang, S.S., 1992. Excess argon, crustal fluids and apparent isochrons from crushing K-feldspar. Earth Planet. Sci. Lett. 110 (1–4), 193–211.

Wang, S.S., 1983. Age determinations of $^{40}Ar/^{40}K$, $^{40}Ar/^{39}Ar$ and radiogenic ^{40}Ar released characteristics on K–Ar geostandards of China. Sci. Geol. Sin. (4), 315–323 (in Chinese with English abstract).

Wang, X.D., Ni, P., Jiang, S.Y., Zhao, K.D., Wang, T.G., 2010. Origin of ore-forming fluid in the Piaotang tungsten deposit in Jiangxi Province: evidence from helium and argon isotopes. Chin. Sci. Bull. 55 (7), 628–634.

Yun, J.B., Wu, H.Y., Feng, Z.H., Mei, L.F., Qiu, H.N., 2010. CO_2 gas emplacement age in the Songliao Basin: insight from volcanic quartz $^{40}Ar–^{39}Ar$ stepwise crushing. Chin. Sci. Bull. 55 (17), 1795–1799.

Zhang, W.L., Hua, R.M., Wang, R.C., Li, H.M., Qu, W.J., Ji, J.Q., 2009. New dating of the Piaotang granite and related tungsten mineralization in southern Jiangxi. Acta Geol. Sin. 83 (5), 659–670.

Zhang, R.Q., Lu, J.J., Lehmann, B., Li, C.Y., Li, G.L., Zhang, L.P., Guo, J., Sun, W.D., 2017. Combined zircon and cassiterite U–Pb dating of the Piaotang granite-related tungsten-tin deposit, southern Jiangxi tungsten district, China. Ore Geol. Rev. 82, 268–284.